Check for updates

Micromachined phase-shifted array-type Mirau interferometer for swept-source OCT imaging: design, microfabrication and experimental validation

C. GORECKI,[1,*] **J. LULLIN,**[1] **S. PERRIN,**[1] **S. BARGIEL,**[1] **J. ALBERO,**[1] **O. GAIFFE,**[1] **J. RUTKOWSKI,**[1] **J. M. COTE,**[1] **J. KRAUTER,**[2] **W. OSTEN,**[2] **W.-S. WANG,**[3] **M. WEIMER,**[3] **AND J. FROEMEL**[3]

[1]*FEMTO-ST Institute (UMR CNRS 6174, UBFC), 15B avenue des Montboucons, 25030 Besançon, France*
[2]*Institut für Technische Optik, Universiät Stuttgart, Pfaffenwaldring 9, 70569 Stuttgart, Germany*
[3]*Fraunhofer Institute for Electronic Nanosystems, Technologie Campus 3, 09126 Chemnitz, Germany*
[*]*christophe.gorecki@femto-st.fr*

Abstract: OCT instruments permit fast and non-invasive 3D optical biopsies of biological tissues. However, they are bulky and expensive, making them only affordable at the hospital and thus, not sufficiently used as an early diagnostic tool. Significant reduction of system cost and size is achieved by implementation of MOEMS technologies. We propose an active array of 4x4 Mirau microinterferometers where the reference micro-mirrors are carried by a vertical comb-drive microactuator, enabling the implementation of the phase-shifting technique that improves the sensitivity and eliminates unwanted interferometric terms. We focus on the design of the imaging system, the microfabrication and the assembly of the Mirau microinterferometer, and the swept-source OCT imaging.

1. Introduction

Nowadays, the micromachining technologies are well matching the needs of biomedical applications of modern optical metrology. Applications such as micro-spectrometers [1], on-chip confocal microscopy [2] and micro-catheters [3] for in-vivo tissue scanning are some examples where potential sensing is increased by using MOEMS (micro-opto-electro-mechanical systems) technologies. The ability to fabricate micromachined micro-mirrors, scanners and other microoptical elements on the order of several hundreds of micrometers in size has stimulated research into new instrumental applications. Low-inertia scanners that deflect light using a MEMS component of small mass have suited features such as high-scanning speed and accuracy positioning at low cost, without the degradation of the measurement resolution. The cost effectiveness of all these devices permits portability, therefore, increasing the usability and serviceability of medical instruments. Also, an increasing demand allowing the reduction of size and cost as well as several new sensing challenges, such as imaging inside of the human body, have made the miniaturization of interferometric systems an important issue [4,5].

MOEMS and MEMS components can be stacked using a multi-wafer vertical integration method to build array-type microinterferometers and microscopes. The potential of such integration has been demonstrated recently for an electrostatically tuned grating microinterferometer [6] as well as for a miniature laser Twyman-Green interferometer [7] and 5x5 array of low-coherence Mirau microinterferometers [8], used for a massively parallel in-line inspection of MEMS.

Among of the instruments that can benefit from the significant improvement in equipment efficiency and quality of patient diagnosis, resulting from incorporation of MOEMS

technologies, are the Optical Coherence Tomography (OCT) imagers [9]. OCT is a powerful biomedical imaging technology offering the cross-sectional imaging with 1-10 μm resolution and 1-3 mm imaging depth. It is a technique of low-coherence interferometry where the interferometer acquires the interference signal issued from each single scan point reflected by a transparent sample and records it as a depth profile (A-scan). Series of A-scans across the sample permits a cross-sectional reconstruction where a 3D volumetric image is obtained by combining multiple cross-sections. Various interferometry configurations are in use for OCT but the main configuration remains the Michelson interferometer [10]. In a Michelson interferometer objective, suitable for small magnifications, a beam splitter cube and a reference mirror are inserted between the objective and the sample [11]. Michelson interferometer requires a long working-distance objective because at magnifications higher then 50X, the working distance becomes too short to squeeze in a beam splitter cube. The Linnik interferometer is well adapted for high magnifications (100X-200X) with an objective of large numerical aperture (NA) but a short working distance. This is a complex configuration because a beam splitter cube directs the beam into two matched and similar objectives; the first beam is directed towards the reference mirror and the second one is directed towards the test surface. The Mirau interferometric objective is the favorite configuration for its medium and high magnifications (10X-100X) since only a single objective is needed. The advantage of such a configuration is to place a reference mirror in the center of the objective lens, and interposing a semi-transparent plate between the reference mirror and the specimen, producing a compact package. Because of its particular architecture, the Mirau interferometer is well suited to be vertically integrated at wafer-level by MOEMS-based technologies. The main drawback of Mirau configuration consists in the obscuration of central part of image by the reference mirror. At magnifications lower than 10X with corresponding smaller NA values, the central obscuration of Mirau interferometer can be significant. In this case, using higher numerical apertures can only minimize the presence of the central obscuration. The axial and lateral resolutions of a Mirau interferometer are well suited for the exigencies of OCT imaging of the living tissues and its range of working distances is well adapted to the requirements of in-vivo measurements such as the diagnosis of skin pathologies. In dermatology, the majority of the OCT systems are bulk microscopes, performing the serial measurements and presenting a limited potential for miniaturization. A need for miniature and low-cost instruments is thus enhanced, enabling to read the data in parallel by a matrix of probe sensors. This is the core of the present contribution. In spectral domain OCT, the implementation of MOEMS technologies offers not only the size and cost reduction, but also the implementation of actuated micro-mirrors for the building of an optical phase-shifter allowing the reduction of the parasitic terms of interference signal and improving the quality of OCT images [12].

In this paper, we focus on the implementation of an active and array-type micromachined Mirau microinterferometer for swept-source OCT (SS-OCT) imaging. First, we present the architecture of the Mirau microinterferometer where the reference micro-mirror is integrated on top of a vertical comb-drive actuator, and we define its main functional parameters. Second, we focus on fabrication process of each micro-optical and MEMS building block as well as of the complete assembly. To verify the imaging quality of the resulting OCT microsystem, three transparent samples are measured and the interest of phase-shift performed via the MEMS actuator is demonstrated.

2. Design and methods

2.1 Design and specifications of the Mirau microinterferometer for SS-OCT imaging

The matrix of active Mirau microinterferometers is designed to be a core component of our SS-OCT microsystem, as detailed in Ref. 13. The experimental set-up is shown in Fig. 1(a). The illumination block includes a commercial swept-source laser (ESS-840 Exalos) having a central wavelength of $\lambda_c = 840$ nm, a spectral bandwidth of $\Delta\lambda = 78$ nm and an A-scan

frequency of 110 kHz. The incident light beam is collected by an array of 4x4 Mirau microlenses and directed towards the sample to be measured. For each single-channel interferometer the collected light passes through a thin beam-splitter plate that reflects a part of it back to a moving reference micro-mirror integrated on top of the MEMS actuator, while the rest of light is transmitted towards the sample to be measured. The beams reflected by the sample and by the reference micro-mirror interfere, generating an interference pattern, and are directed by a 4x4 array of microlenses towards a high-speed camera after the transmission by a cube beam-splitter. The square-pixel size of the camera is 12 µm and the frame rate is set to 4 kfps. The vertical actuation of Mirau reference micro-mirrors allows a phase shifting increment to be achieved. Being actuated at the resonance frequency by sinusoidal driving signal, the MEMS-based system enables a rapid measurement of the interferograms.

The architecture of the active Mirau interferometer is shown schematically in Fig. 1(b). The device consists of a series of vertically stacked components: a doublet of plano-convex microlenses, an electrostatically driven vertical comb-drive actuator carrying the array of Mirau reference micro-mirrors, a spacer and a planar beam splitter plate. In the following discussion, W1 represents the microlens doublet matrix, W2 represents the Z microscanner, and W3 is the spacer while W4 represents the beam-splitter wafer. To build the Mirau interferometer, the doublet of microlenses has been selected instead of single microlenses [14]. Because of lower optical aberrations, the optical performance achieved by the lens doublet is better than for an individual lens having an equivalent numerical aperture. The assembly of two glass microlens arrays is made by anodic bonding at the wafer-level thanks to their silicon frame resulting from each array fabrication. Such microlens doublets are then well aligned and robust. The diameter of an individual microlens is 1.9 mm and the array pitch is 2 mm. The focal length of a microlens doublet is 7.5 mm, giving a numerical aperture of 0.1.

The transverse resolution of OCT imaging is defined by the effective numerical aperture of the focusing lens and is limited to 6.3 µm. Moreover, the axial resolution of OCT imaging is 6.2 µm that is determined by the optical performance of the light source, i.e. the central wavelength and the swept range of the laser source. The OCT configuration allows a depth of penetration of 0.6 mm with a sensitivity in the range of 70-85 dB.

The key element of Mirau interferometer is the vertical microscanner W2. The design and the fabrication of this silicon-on-insulator (SOI)-based scanner are described in Ref. 15. The microscanner is designed to generate a vertical displacement of a large platform with an array of 4x4 reference micro-mirrors of the Mirau interferometer, as shown in Fig. 1(c). Here, the micro-mirror platform is represented with micro-mirrors 1-4 whose mechanical characterization is provided latter. The vertical motion of the whole array of the 4x4 reference micro-mirrors at the resonance frequency of actuator is used to implement the sinusoidal phase-shifted imaging where the displacement can be controlled precisely by in situ position capacitive sensor. In our case, the microscanner is designed to work in transmission, i.e. the areas around the micro-mirror are transparent. The platform is thus formed by 16 apertures made in a 40-µm thick device layer of the SOI wafer and is structured with small holes in order to decrease its weight. A honeycomb structure is chosen for its good trade-off between mass and stiffness, preventing the possible vertical deformation of the platform (see the image of Fig. 1c). The size and the shape of the micro-mirrors are defined by the optical design of the Mirau microinterferometer as a 400x400 μm^2 square surface. Important design issue concerns the minimization of the obscuration created by the reference micro-mirror in the center of the light beam.
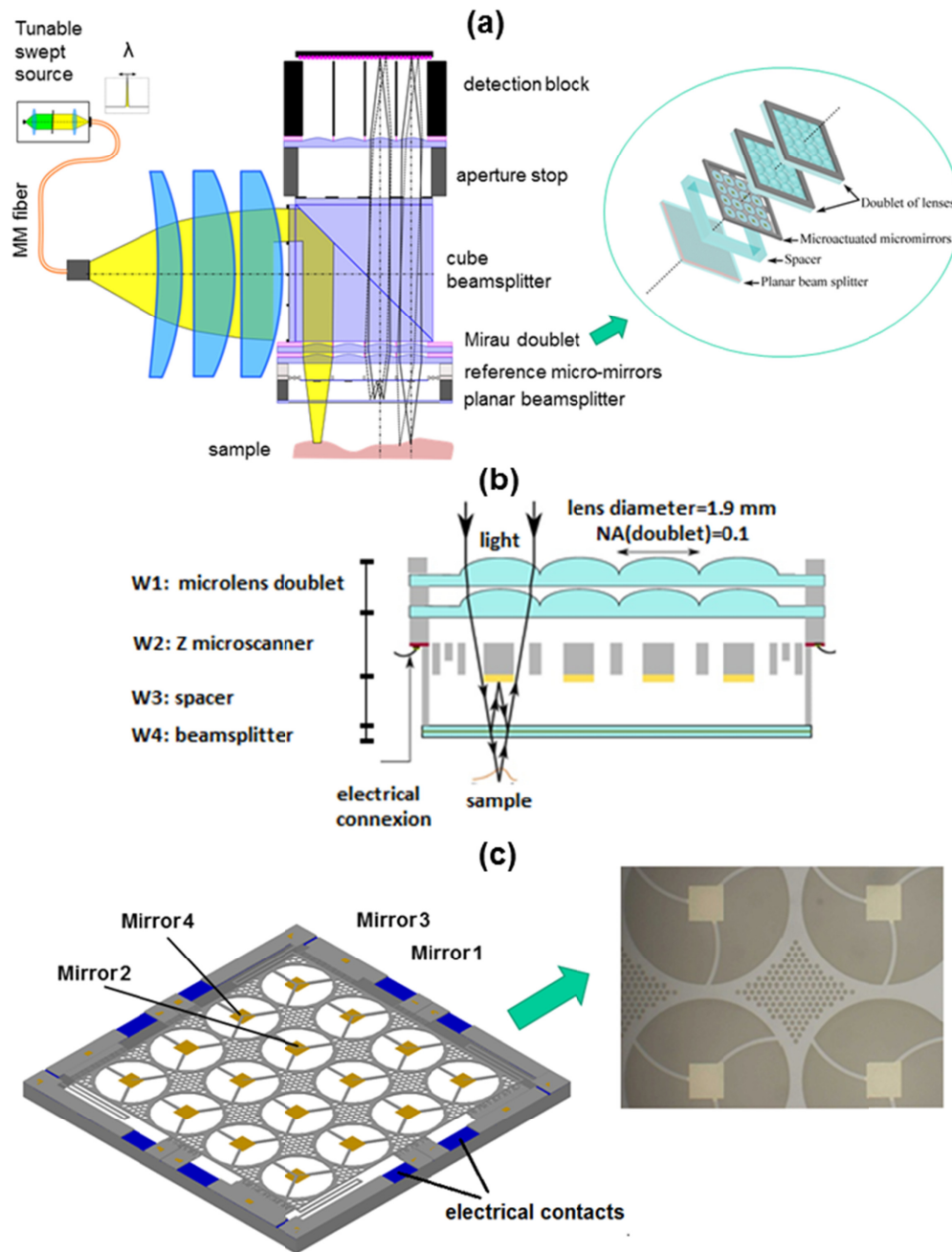
Fig. 1. Design layout of the SS-OCT microsystem: (a) SS-OCT setup; (b) schematic cross-sectional view of 4x4 array of active Mirau micro interferometers; and (c) a focus on 3D view of electrostatic vertical microscanner with an array of suspended reference micro-mirrors and a zoom on the honeycomb structure.

The size of a micro-mirror corresponds to a transmission of the mirror plane of 94% (the clear aperture around the micro-mirror having a diameter of 1.84 mm). The reference micro-mirrors of Mirau interferometer are suspended by a system of spider legs. The presence of suspension legs obscures the light beam and creates diffraction effects. We demonstrated in

Ref. 16 that their impact is negligible in a certain range of design parameters such as their width, number and radius of curvature. Thus, the suspensions are chosen to be 50-μm wide and the optimal number of legs is three. They have a radius of curvature, which equals the clear aperture diameter around the micro-mirror. Finally, the platform is dimensioned to the array of micro-mirrors, vertically aligned with the microlenses, forming an 8x8-mm^2 structure.

For the implementation of the phase-shifting algorithm, the microscanner is driven by sinusoidal signal $V_S = V_{DC} + V_M \sin(\omega_o t)$ at its resonance frequency $f_o = 485$ Hz. The maximal required amplitude of the micro-mirror displacement corresponds to the peak-to-peak amplitude of 352 nm. However, the microscanner can provide much higher displacement in the range of a few micrometers both in static as well as in dynamic modes.

Further, the 3-mm thick spacer W3, made of glass, permits to adjust both the positions of microlens focal plane and the localization of planar beam-splitter plate W4. The beam-splitter is fabricated by deposition of a thin layer of titanium dioxide having a transmission/reflection ratio of 70/30.

The continuously reconstructed tomography volume is performed by stitching the complete optical head of Fig. 1(a), i.e. the 4x4 single-channel interferometers, via a system of bulk actuators. The mechanical displacement of the Mirau-array is able to cover overlapping regions.

2.2 Fabrication and assembly of building blocks of Mirau microinterferometer

This Section illustrates the process flow and assembly of functional components of the active Mirau interferometer.
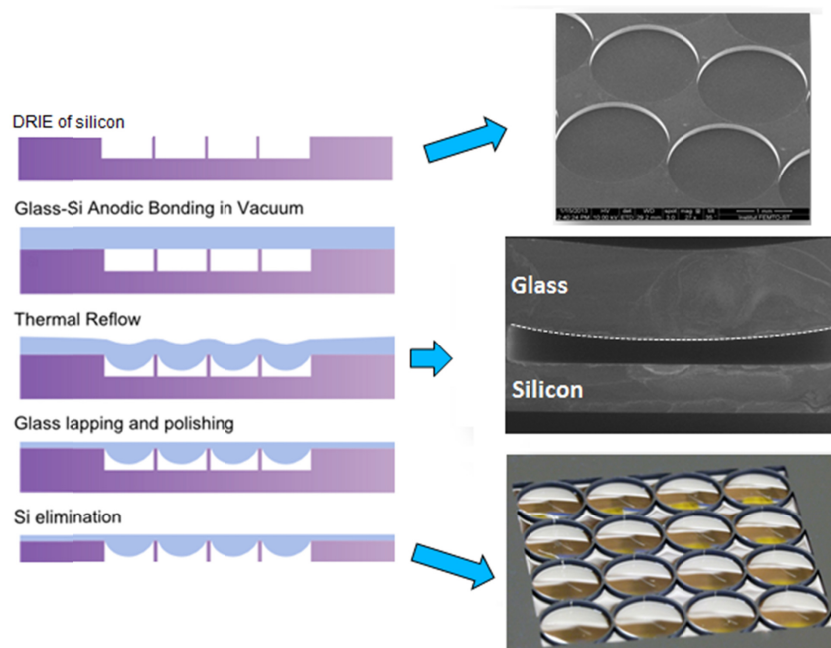

Fig. 2. Wafer-level process of array-type plano-convex glass microlenses.

For the individual array of plano-convex glass microlenses, the fabrication flowchart is shown in Fig. 2, according to [17]. First, a silicon substrate with a thickness of 525 μm is spin-coated with a positive photoresist. The photoresist is patterned by UV photolithography to form circular apertures 1.9 mm in diameter, following by etching of cavities into silicon by deep reactive ion etching (DRIE), as shown in the top photography of Fig. 2. The photoresist

is removed and a 100-nm thick layer of silicon oxide (SiO_2) is thermally grown on the silicon. After oxidation, the silicon wafer is sealed to a Borofloat 33 glass wafer by anodic bonding in a vacuum chamber, producing a pressure in the range of 10^{-3} mbar inside the silicon cavities. The silicon-glass set is then heated up to a temperature between the annealing and the softening point of glass (560°C and 820°C, respectively). Thanks to the pressure difference between the cavities and the furnace chamber, the glass is attracted towards the bottom of the cavity producing a spherical shape, as demonstrated in the central photography of Fig. 2. The topside glass is afterwards grinded and polished to achieve an optical quality flat surface. Finally, the backside of the silicon is removed in KOH to release the convex side of the microlenses. The resulting array of microlenses is shown in the lower photography of Fig. 2.

The fabrication flowchart of the Z microscanner is presented schematically in Fig. 3. This is detailed in [15]. The fabrication starts by the thermal oxidation of SOI wafer (step a). The process continues with the creation of the comb fingers based on a two-step of DRIE etch, silicon dioxide is used as a first mask and a photoresist as the second mask (steps b-c). In the same DRIE steps, the suspensions of the micro-mirrors are formed in the device layer of SOI wafer (steps d-e). The wafer is then oxidized (step f) to protect the front side during the backside etching. The structure is released from the backside by hydrofluoric acid (HF) vapor etching of the buried oxide (BOX) layer (step g). Finally, the micro-mirrors and the metal contact pads are deposited through a shadow mask by sputtering (step h). The photography of Fig. 3 illustrates a wafer of released Z microscanners, shown on the side of the micro-mirror platform.
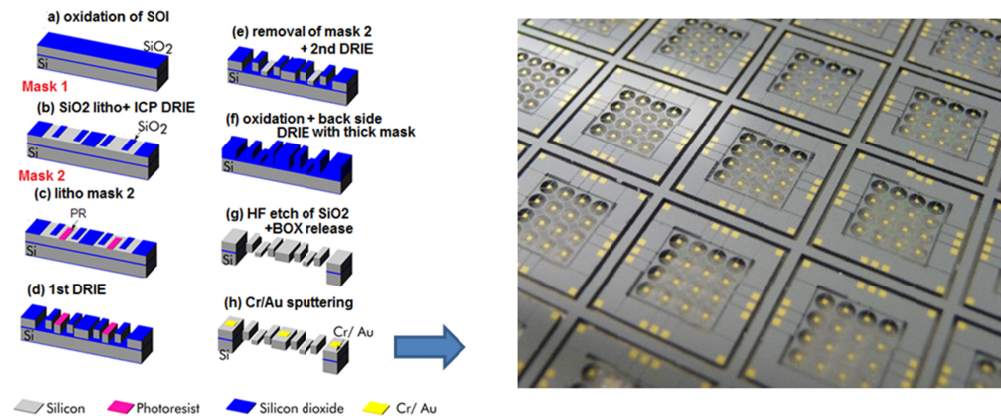

Fig. 3. Flow-chart of Z microscanner and a view of the micro-mirror platform.

Fig. 4. illustrates the different steps of fabrication of Z microscanner.

A complete Mirau interferometer is a stack of seven wafers, composed of heterogeneous materials. In addition, the choice of bonding technology should consider material and process compatibility of the Mirau stack as well as alignment accuracy to ensure optical performances of the Mirau interferometer. Among various bonding techniques, anodic bonding is preferred for assembly of this Mirau stack because of less complex process design, high bonding strength and medium bonding temperature. During the anodic bonding, substrates are heated to 350-400°C and a voltage between 400 V and 1500V is applied for a time up to 90 min. These process parameters are compatible with metallic and dielectric layers composing the Z microscanner and the beam-splitter. Moreover, since the electrostatic Z microscanner is sandwiched between two glass wafers, i.e. microlens doublet wafers W1 and the spacer W3, the integration process must also provide a solution for electrical interconnections, taking into account the maximum value of the pull-in voltage. The requirement of dermatology application is to limit this voltage up to 50 V.
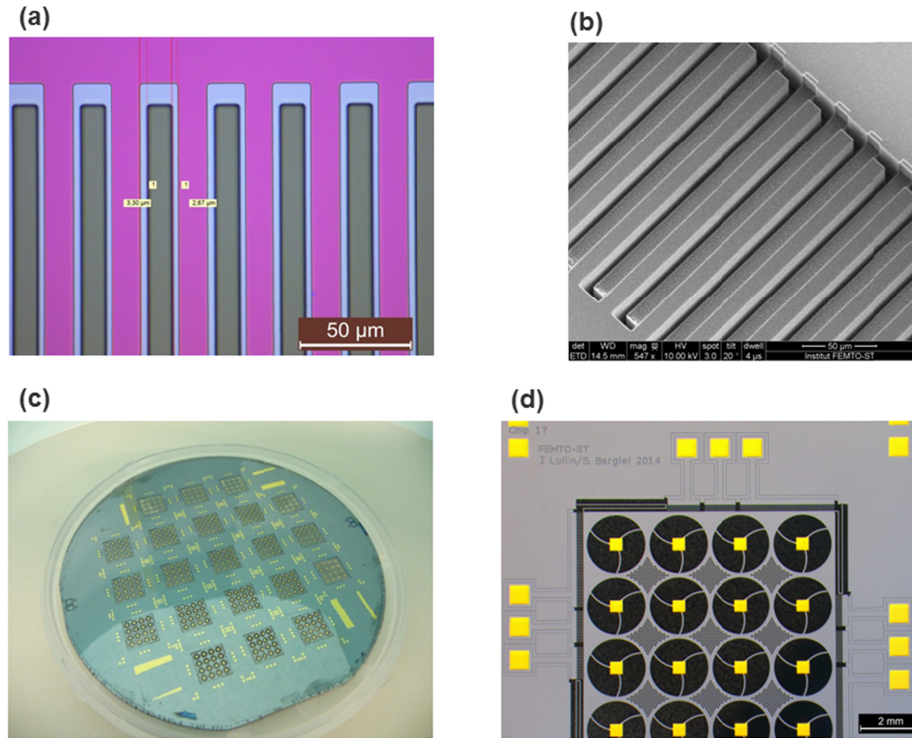
Fig. 4. Illustration of process flow steps for the Z microscanner: (a) first DRIE etch (step d): structuration of comb-drive fingers; (b) removal of Mask 2 and second DRIE (step e): view of comb-drive fingers; (c) wafer of released Z microscanners (step g); and (d) deposition of contact pads (step h).

Figure 5(a) shows the cross section of Z microscanner where the bond interfaces are* plotted in red color (interfaces I, III, II, IV). The numbering of bonding interfaces corresponds to the order of bonding operations. The Mirau microinterferometer consists of two probing wafers (W1a + b, W1c + d), carrying an array of microlenses, a SOI wafer of Z microscanner (W2), carrying an array of reference micro-mirrors, a spacer (W3) used for focus adjustment, and a beam-splitter wafer (W4). Each microlens wafer consists of a stop silicon wafer bonded with a glass wafer. For a Mirau interferometer, the most fragile and sensitive part is the Z microscanner W2. To minimize influences of temperature and bonding process on W2, the functional wafers are sequentially stacked and bonded according the bonding procedure detailed in Ref. 18. First, W3 and W4 wafers are bonded (interface I). To make the anodic bonding between W3 and W4 possible, W4 is covered with a thin Al layer and then W3 and W4 are bonded together. After the bonding, the Al layer is etched away to keep the optical path free. The W3/W4 stack is then bonded to W2 (interface II). The last step consists to bond the microlens doublet W1 with the W2/W3/W4 stack (interface III). The microlens doublet consists of two separate wafers where each microlens wafer contains a stop wafer in silicon (W1a, W1c) and a glass wafer (W1b, W1d). Silicon and glass wafers are anodically bonded (interface IVa and IVc, respectively) to prepare the individual microlens wafer. After fabrication of the microlens wafer, two microlens wafers, W1a + b and W1c + d, are bonded anodically to form a microlens doublet (interface IV). For each microlens wafer, a silicon wafer is bonded with glass wafer and the total thickness is 4.37 mm. The final step of bonding W1 with W2/W3/W4 stack is carried out, producing a wafer stack of total thickness of 5 mm.

The whole wafer stack W1/W2/W3/W4/W5 is aligned with an accuracy of +/− 16 μm. Figure 5(b) shows anodically bonded wafer of Mirau active interferometers.
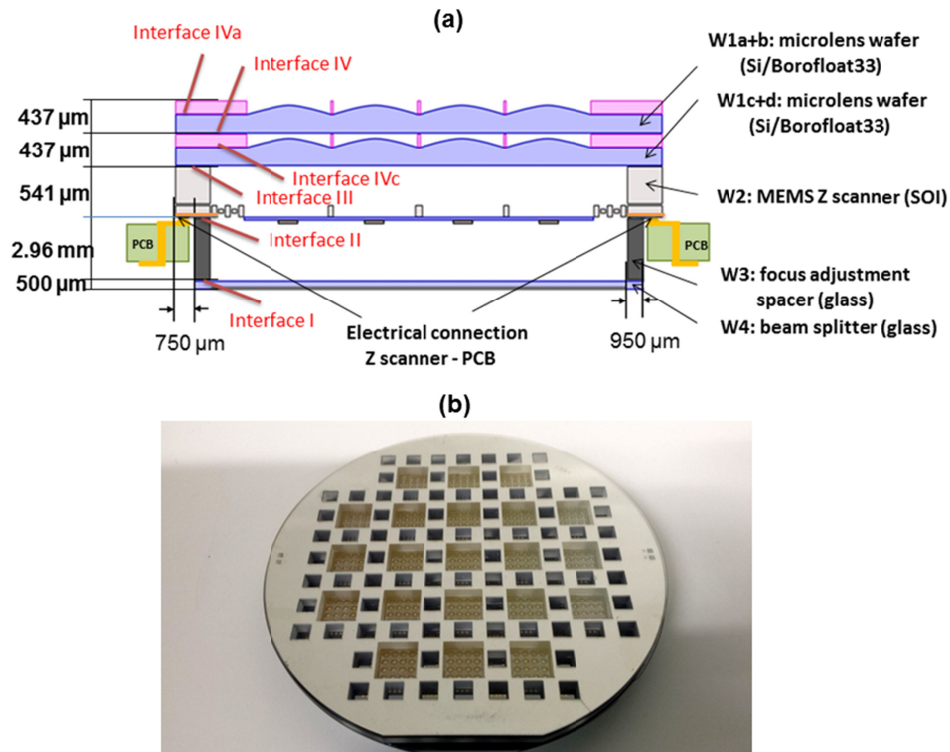

Fig. 5. Assembly results: (a) bonding interfaces and electrical connection strategy, b) anodically bonded Mirau wafer stack.

After the assembly of Mirau wafer stack, we obtained the individual chips by picosecond laser cutting. The dicing operation is challenging because of the presence of isolation trenches, etched into the device layer of SOI wafer of Z microscanner. Indeed, these trenches prevented the final bonded stack to be completely hermetic. The dicing strategy combines trench filling and two-step laser cutting, separating this non-hermetic Mirau-interferometer wafer stack into individual chips. The footprint of these chips is 15x15 mm^2 whereas the overall thickness is about 5 mm.

To drive the electrostatic Z microscanner, which is sandwiched between microlens doublet wafers W1 and the spacer W3, electrical interconnections are performed, according the schema shown in Fig. 5(a). The Z microscanner is mounted on the printed circuit board (PCB). The PCB allows the electrical connection with the electrodes of Z microscanner through the bonding interface II. Here, the yellow lines are connections and vias of PCB. The brown lines are used bumping technology combines the PCB with silver-filled epoxy bumps to perform the flip chip bonding of chips. Figure 6 shows one diced matrix of Mirau microinterferometers mounted on the PCB and shown from the topside where the microlens array is visible.
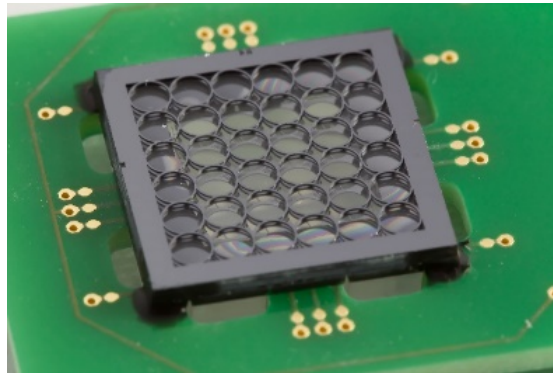
Fig. 6. View of a PCB-mounted chip of Mirau interferometers, shown from the microlens side.

3. Results and discussion

To validate performances of the MOEMS-based Mirau interferometer in OCT imaging both optical and mechanical characterizations have been performed.

First, the lateral resolution has been evaluated experimentally by imaging a 1951 USAF resolution target. The linewidth of smallest line pair on the USAF target, which is well resolved, is 6.2 µm.

Figure 7(a) shows two cross sections of the intensity Point Spread Function (IPSF) of one selected Mirau interferometer after assembly [19]. The image at the left of Fig. 7(a) represents the axial irradiance distribution (XZ slice) measured along the optical axis. The image on the right of Fig. 7(a) corresponds to the YX slice measured at the focal point. The FWHM value of the IPSF at the center of the focal plane is 5 µm, which confirm the previous optical characterization of the lateral resolution. Moreover, the focal length of the doublet equals 7.65 mm and the depth of field is around 400 µm.

The actuation performance of the Z microscanner has been tested using the Doppler vibrometry module MSA500 from Polytec. We measured the actuator static displacement as a function of applied voltage between 0 and 40 V. For 40 V the measured amplitude of the static displacement is around 1.75 µm. The first resonance frequency of the Z microscanner is 485 Hz, corresponding to a piston mode motion of the scanner. This mode is precisely used for the actuation of the vertical microscanner to perform the phase modulation. The quality factor of the vertical microscanner is around 64, giving thus an excellent basis for robust and stable actuation. Figure 7(b) shows the micro-mirror displacement under a sinusoidal excitation, demonstrating the targeted peak-to-peak amplitude of 352 nm. This function is obtained by applying a voltage $V_S = 2.5 + 1.5\sin(\omega_0 t)$ V for all the actuators, where ω_0 is the first resonance pulsation. As the electrostatic force is proportional to the square of the voltage, the applied voltage is a sum of a DC force, a force proportional to $\sin(\omega_0 t)$ and a force proportional to $\sin(2\omega_0 t + \pi/2)$.

For the implementation of phase shifting algorithm, it is important to know the displacement amplitude of all the reference micro-mirrors in the same array. The dynamic displacement of the platform at resonant frequency was investigated at different points of the platform, i.e. at the position of the four micro-mirrors of Fig. 1(c), forming a quarter of the platform. The vertical displacement of the reference micro-mirrors was measured under dynamic driving voltage at the center position of the four micro-mirrors (Mirror 1-Mirror 4). Here, the measured displacement is much larger than the targeted one (352 nm), demonstrating the potential of this microscanner for medical imaging applications, for which small voltages are particularly important since the device is in contact with the patient body. The displacement of the micro-mirror in the middle of the platform (Mirror 2) is 70 nm higher than the one next to the spring (Mirror 3) because of the vertical mechanical deformation of

the suspended platform. We demonstrated that such dispersion is not critical for the phase-shift efficiency, especially in case of sinusoidal modulation of the reference mirror [20].
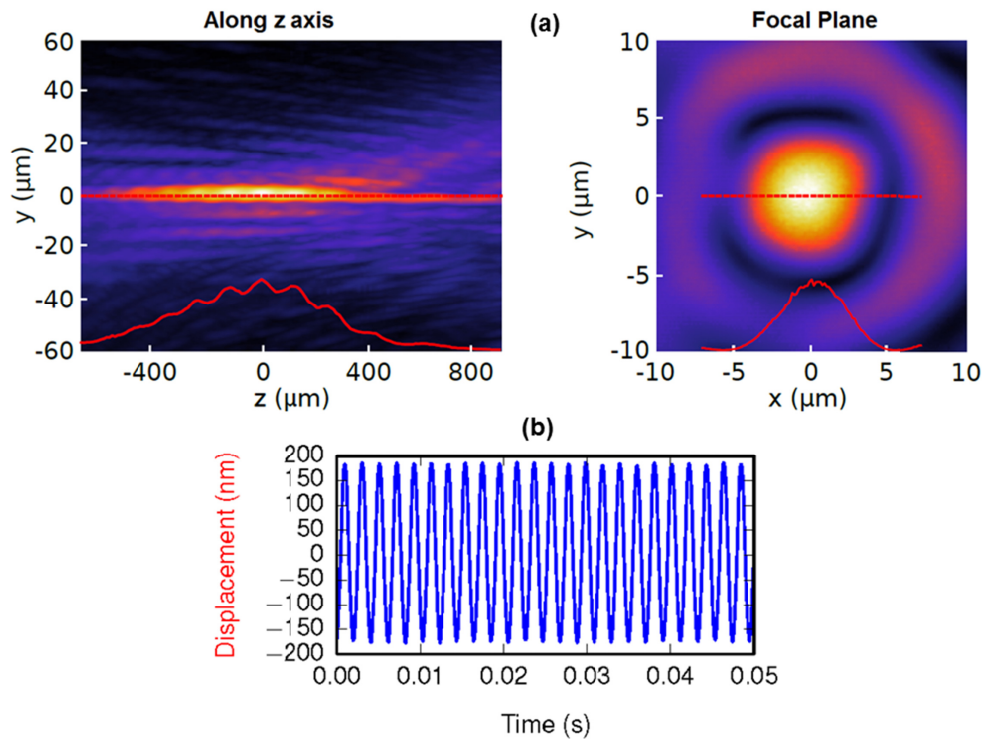

Fig. 7. Opto-mechanical characterization: (a) measured IPSF with an YZ slice along the optical axis and XY slice at the focal plane; and (b) micro-mirror displacement under a sinusoidal excitation obtained at resonance frequency.

Standard SS-OCT suffers from the presence of artefacts such as the autocorrelation terms, overlapping micro-mirror images as well as the DC terms that obscure the true OCT signal of the measured sample by degrading the sensitivity and signal-to-noise ratio. By use of phase shifting it is possible to remove those parasitic terms and to double the depth range. The goal of the present Section is to demonstrate the strong interest to use the Z microscanner of Mirau interferometer as a phase shifter. Several phase-shifting devices have been developed to eliminate the parasitic terms of interference signal: piezoelectric actuators [21], electro-optic phase modulators [23], electrostatic comb-drive actuators [24], and arrays of individually actuated surface-micromachined micro-mirrors [25].

The demonstration of proposed phase-shifting method is made by imaging a reflective surface of a mirror with one-channel Mirau microinteferometer. Figure 8(a) shows the A-scan plot of this sample obtained without the phase shifting by applying only a Fourier transform to the spectral signal. The true OCT image of sample (S) is obscured by the overlapping with other artefact terms such as the DC noise term (DC) that contains the energy of the signal and which is centered onto the zero frequency, and the sample complex conjugate (S*). Moreover, the lack of antireflective coating on the planar beam-splitter produces parasitic reflections, generating an autocorrelation term (A_{BS}) of the beam splitter. This last term is located at a depth corresponding to the optical thickness of such substrate ($\pm$ 720 µm = 500 µm x n_{SiO2}). The back surface of the beam-splitter plate, then located within one interferometer arm, is also responsible for a replica of the sample term (SR), shifted by 720 µm until the Fourier space. Its complex conjugate term (SR*), therefore, appears near to the sample term, making

the interpretation of the A-scan complex. Controlled actuation of the reference micro-mirror allows to record $\pi/2$ phase-shifted images. Figure 8(b) shows the A-scan obtained after application of a simple two-frame phase shift algorithm based on the acquisition of two spectral interferograms at 0° and $\pi/2$. This simple combination of two shifted spectra is sufficient to subtract the sample conjugate terms (true sample S* and its replica SR*) while improving slightly the signal-to-noise-ratio. However, the autocorrelation terms, as well as the DC term, are not removed by the two-frame phase-shift. Hence, Fig. 8(c) shows the A-scan after filtering performed by a four-frame phase-shift algorithm. We used a classical four-step algorithm with the phase shift of 0, $\pi/2$, π and $3\pi/2$. Here, only the true OCT signal (S) is recovered along with its shifted replica (SR). Consequently, such algorithm improves both the signal-to-noise ratio and the measurement range.
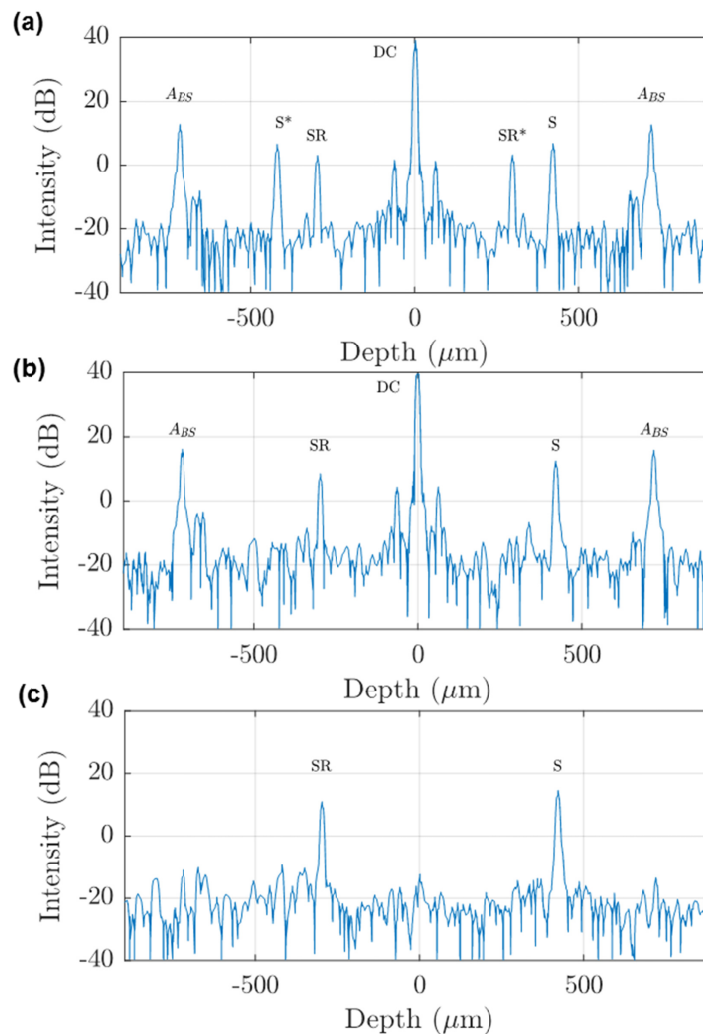

Fig. 8. SS-OCT A-scan plots obtained: (a) in absence of phase-shift; (b) with a 2-frame phase-shift algorithm; and (c) with a 4-frame phase-shift algorithm.
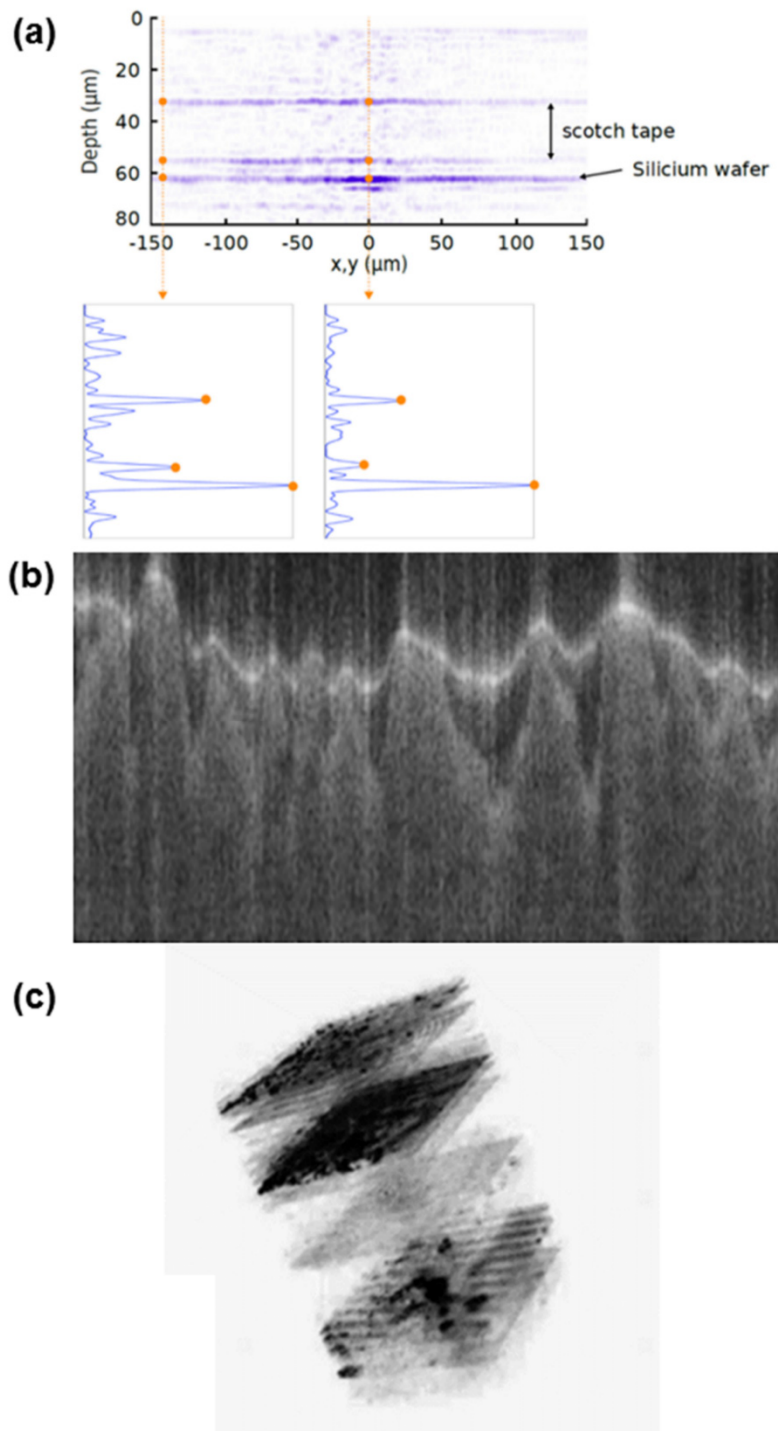
Fig. 9. SS-OCT images: a) 2D cross-sectional image from the multi-layer scotch tape; (b) 2D cross-sectional image from 4-mm long sample made of scratched paint covered with varnish; and (c) 3D image of onion slices.

The first experimental demonstration of SS-OCT imaging has been made using a scotch tape stick onto a silicon wafer. Figure 9(a) shows the acquired cross-section image where the

three different layers appear. This image is completed by two A-scan plots, which are extracted from the center and from the edge of the image. As the OCT image was obtained without the phase-shift, artifact peaks appear around the three main ones, indicated by orange dots. The B-scan reconstruction was retrieved along 300 µm lateral field of view. A small decrease of the sensitivity can be seen at the edge of the cross-sectional image. The decrease of the signal-to-noise ratio at the border is estimated to be −5 dB, compared to the main peak, corresponding to the signal from the wafer layer. Despite this signal loss, the two diopters generated by the scotch-tape and the surface of the wafer can be retrieved. The measured height of the scotch-tape is 22 µm. The sensitivity of this OCT image is in the range of 60 dB.

Second, we selected a diffusive sample optically similar to the sample of pig skin, which is representative of what is desired in dermatology. For a dermatologist a good OCT imager is capable of revealing the fine details of skin tissue microstructures with a lateral resolution of less than 10 µm and an imaging depth of less than 1 mm. Figure 9(b) represents a cross-sectional OCT image of a layer of scratched paint covered with varnish. Here, the sample was mounted on a mechanical stage, insuring a linear displacement on 4 mm with a precision of 1 µm. Scratches under the varnish are clearly visible. The thickness of the varnish's layer is about 300 nm. The estimated sensibility is around 80 dB.

Finally, we measured OCT images of an onion slice to demonstrate the feasibility for 3D imaging of biological specimens. Figure 9(c) shows the microscopic structure of an onion slice where a 3D volumetric image of $300 \times 300 \times 600 \, \mu m^3$ is reconstructed. The 3D reconstruction reveals inner sample structure corresponding to the different separated layers. We estimate the sensitivity of this image to be in the range of 35-40 dB.

4. Conclusions and perspectives

MOEMS technology combining MEMS and micro-optics is well suited for manipulating light with different ways to scan, steer or modulate the beams, offering batch-fabricated microsystems at lower cost. A number of MOEMS technology demonstrators have been developed for imaging needs of the medical market.

In this paper, we reviewed the design, the fabrication process and experimental results of an active micromachined array-type Mirau interferometer. The Mirau interferometer includes the electrostatic vertical microscanner carrying an array of reference micro-mirrors, being the key element of a SS-OCT imager. The technology of each functional part of this miniature multi-channel Mirau microinterferometer and the integration schema are described and discussed. In particular, the 3D assembly offers an integration platform for complex MOEMS and allows the effective integration of various heterogeneous technologies, disposed in vertically stacked building blocks (glass microlens, MEMS actuator, beam splitter) in a minimum space. The presented results demonstrate experimentally the proof-of-concept of our approach.

Thanks to the optimized design of this vertical architecture, several original technologies are proposed, offering the integrity of MEMS microactuators assembled with microoptics. This approach offers a low level of residual stress and provides a miniaturized and low-cost solution to create highly accurate microsystem for OCT imaging, composed by several hybrid components. The proposed OCT microsystem, presenting the lateral resolution of 6.3 µm, is well suited for the early diagnosis of cutaneous pathologies. The OCT microsystem is rapid because of the array-type architecture, and has the attractive attributes of simplicity and low cost.

When operating working in the regime of full-field OCT, realizing direct imaging with the help of the complete array of Mirau interferometers, the microsystem has a field of view of 8x8 mm^2. This field of view is larger than the field of view of commercially available OCT microscopes, widely used in dermatology. Thus, the field of view of Vivo Sights system from Michelson Diagnostic is 6x6 mm^2 while that of Afga HealthCare Skinell is 1.8x1.5 mm^2. In future works, the full benefit of full field OCT imaging will be obtained by the improvement

of the illumination block with the implementation the Köhler illumination. Other step of development will include the improvements of optical quality of Mirau components, including in particular the design and fabrication of an improved version of focusing microlenses with AR coatings.

Disclosures

The authors declare that there are no conflicts of interest related to this article.

References

1. A. Rissanen, A. Akujärvi, J. Antila, M. Blomberg, and H. Saari, "MOEMS miniature spectrometers using tuneable Fabry-Perot interferometers", J. Micro/Nanolith. MEMS MOEMS **11**(2), 023003 (2012).
2. T. D. Wang, M. J. Mandella, C. H. Contag, and G. S. Kino, "Dual-axis confocal microscope for high-resolution in vivo imaging," Opt. Lett. **28**(6), 414–416 (2003).
3. A. D. Aguirre, P. R. Hertz, Y. Chen, J. G. Fujimoto, W. Piyawattanametha, L. Fan, and M. C. Wu, "Two-axis MEMS scanning catheter for ultrahigh resolution three-dimensional and En Face imaging," Opt. Express **15**(5), 2445–2453 (2007).
4. L. Fan, W. Piyawattanametha, M. C. Wu, A. D. Aguirre, P. R. Herz, Y. Chen, and J. G. Fujimoto, "High-resolution 3D OCT imaging with a MEMS scanning endoscope," Proc. SPIE **5719**, 140–143 (2005).
5. A. P. Lee, C. F. McConaghy, G. Sommargren, P. Krulevitch, and E. W. Campbell, "Vertical-actuated electrostatic comb drive with in situ capacitive position correction for application in phase shifting diffraction interferometry," J. Microelectromech. Syst. **12**(6), 960–971 (2003).
6. O. G. Karhade, F. L. Degertekin, and T. R. Kurfess, "SOI-based micro scanning grating interferometers: device characterization, control and demonstration of parallel operation," J. Micromech. Microeng. **18**(4), 045007 (2008).
7. M. Kujawinska, K. Gastinger, M. Jozwik, K. H. Haugholt, C. Schaeffel, and S. Beer, "An interferometric test station for massive parallel inspection of MEMS and MOEMS," Photonics Lett. Pol. **1**(2), 58–60 (2009).
8. J. Albero, S. Bargiel, N. Passilly, P. Dannberg, M. Stumpf, U. D. Zeitner, C. Rousselot, K. Gastinger, and C. Gorecki, "Micromachined array-type Mirau interferometer for parallel inspection of MEMS," J. Micromech. Microeng. **21**(6), 065005 (2011).
9. J. Sun and H. Xie, "MEMS-Based Endoscopic Optical Coherence Tomography," Hindawi International Journal of Optics **2011**, 825629 (2011).
10. A. Dubois, *Handbook of Full-field Optical Coherence Microscopy: Technology and Applications* (Pan Stanford Publishing Pte. Ltd., Singapore, 2016).
11. P. J. de Groot and J. F. Biegen, "Interference microscope objectives for wide-field areal surface topography measurements," Opt. Eng. **55**(7), 074110 (2016).
12. R. A. Leitgeb, C. K. Hitzenberger, A. F. Fercher, and T. Bajraszewski, "Phase-shifting algorithm to achieve high-speed long-depth-range probing by frequency-domain optical coherence tomography," Opt. Lett. **28**(22), 2201–2203 (2003).
13. J. Krauter, T. Boettcher, K. Körner, M. Gronle, W. Osten, N. Passilly, L. Froehly, S. Perrin, and C. Gorecki, "Performance analysis of a full-field and full-range swept-source OCT system," Proc. SPIE **9576**, 957609 (2015).
14. J. Albero, S. Perrin, N. Passilly, J. Krauter, L. Gauthier-Manuel, L. Froehly, J. Lullin, S. Bargiel, W. Osten, and C. Gorecki, "Wafer-level fabrication of multi-element glass lenses: lens doublet with improved optical performances," Opt. Lett. **41**(1), 96–99 (2016).
15. J. Lullin, S. Bargiel, P. Lemoal, S. Perrin, J. Albero, N. Passilly, L. Froehly, F. Lardet-Vieudrin, and C. Gorecki, "An electrostatic vertical microscanner for phase modulating array-type Mirau microinterferometry," J. Micromech. Microeng. **25**(11), 115013 (2015).
16. J. Lullin, S. Perrin, M. Baranski, S. Bargiel, L. Froehly, N. Passilly, J. Albero, and C. Gorecki, "Impact of mirror spider legs on imaging quality in Mirau micro-interferometry," Opt. Lett. **40**(10), 2209–2212 (2015).
17. J. Albero, S. Perrin, S. Bargiel, N. Passilly, M. Baranski, L. Gauthier-Manuel, F. Bernard, J. Lullin, L. Froehly, J. Krauter, W. Osten, and C. Gorecki, "Dense arrays of millimeter-sized glass lenses fabricated at wafer-level," Opt. Express **23**(9), 11702–11712 (2015).

18. W.-S. Wang, M. Wiemer, J. Froemel, T. Enderlein, T. Gessner, J. Lullin, S. Bargiel, N. Passilly, J. Albero, and C. Gorecki, "Vertical integration of array-type miniature interferometers at wafer level by using multi-stack anodic bonding," Proc. SPIE **9890**, 989011 (2016).

19. S. Perrin, M. Baranski, L. Froehly, J. Albero, N. Passilly, and C. Gorecki, "Simple method based on intensity measurements for characterization of aberrations from micro-optical components," Appl. Opt. **54**(31), 9060–9064 (2015).

20. S. Perrin, "Development and characterization of an optical coherence tomography micro-system. Application to dermatology", PhD thesis, June 2016, Université de Franche-Comté, Besançon, France.

21. R. A. Leitgeb, C. K. Hitzenberger, A. F. Fercher, and T. Bajraszewski, "Phase-shifting algorithm to achieve high-speed long-depth-range probing by frequency-domain optical coherence tomography," Opt. Lett. **28**(22), 2201–2203 (2003).

22. Y. K. Tao, M. Zhao, and J. A. Izatt, "High-speed complex conjugate resolved retinal spectral domain optical coherence tomography using sinusoidal phase modulation," Opt. Lett. **32**(20), 2918–2920 (2007).

23. J. Zhang, J. S. Nelson, and Z. Chen, "Removal of a mirror image and enhancement of the signal-to-noise ratio in Fourier-domain optical coherence tomography using an electro-optic phase modulator," Opt. Lett. **30**(2), 147–149 (2005).

24. K. Oda, H. Takao, K. Terao, T. Suzuki, F. Shimokawa, I. Ishimaru, and F. Oohira, "Vertical comb-drive MEMS mirror with sensing function for phase-shift device," Sens. Actuators A Phys. **181**, 61–69 (2012).

25. P. Bu, X. Wang, and O. Sasaki, "Full-range parallel Fourier-domain optical coherence tomography using sinusoidal phase-modulating interferometry," J. Opt. A, Pure Appl. Opt. **9**(4), 422–426 (2007).